ACS APPLIED MATERIALS & INTERFACES

Research Article

www.acsami.org

$SrCo_{0.9}Ti_{0.1}O_{3-\delta}$ As a New Electrocatalyst for the Oxygen Evolution Reaction in Alkaline Electrolyte with Stable Performance

Chao Su,[†] Wei Wang,[†] Yubo Chen,[‡] Guangming Yang,[‡] Xiaomin Xu,[‡] Moses O. Tadé,[†] and Zongping Shao*[,†,‡]

[†]Department of Chemical Engineering, Curtin University, Perth, Western Australia 6845, Australia

[‡]State Key Laboratory of Materials-Oriented Chemical Engineering, Nanjing Tech University, Nanjing 210009, China

Supporting Information

ABSTRACT: The development of efficient, inexpensive, and stable electrocatalysts for the oxygen evolution reaction (OER) is critical for many electrochemical energy conversion technologies. The prohibitive price and insufficient stability of the state-of-the-art IrO_2 electrocatalyst for the OER inhibits its use in practical devices. Here, $SrM_{0.9}Ti_{0.1}O_{3-\delta}$ (M = Co, Fe) perovskites with different B-site transition metal elements were investigated as potentially cheaper OER electrocatalysts. They were prepared through a typical sol−gel route, and their catalytic activities for the OER in alkaline medium were comparatively studied using rotating disk electrodes. Both materials show high initial intrinsic activities in alkaline electrolyte for the OER, comparable to the benchmark perovskite-type electrocatalyst $Ba_{0.5}Sr_{0.5}Co_{0.8}Fe_{0.2}O_{3-\delta}$ (BSCF), but $SrCo_{0.9}Ti_{0.1}O_{3-\delta}$ (SCT) possessed more operational stability than $SrFe_{0.9}Ti_{0.1}O_{3-\delta}$ (SFT), even better than BSCF and IrO_2 catalysts. Based on the X-ray photoelectron spectra analysis of the oxidation states of the surface Co/Fe in both SFT and SCT before and after the OER tests, an explanation for their different operational stabilities was proposed by adopting a reported activity descriptor correlated to the e_g occupancy of the 3d electron of the surface transition metal cations in the perovskite oxides. The above results indicate that SCT is a promising alternative electrocatalyst for the OER and can be used in electrochemical devices for water oxidation.

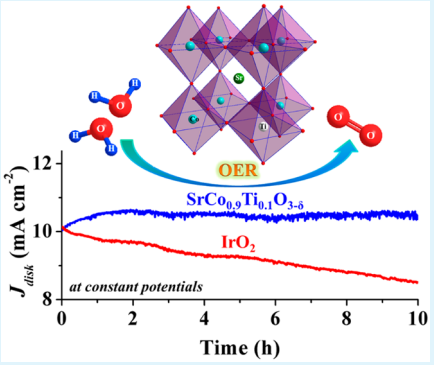

KEYWORDS: *electrocatalysts, oxygen evolution reaction, perovskites, stability, water oxidation*

1. INTRODUCTION

Sustainable energy supply and environmental protection are two of the most important aspects to be considered in the future development of our society, while electrochemical energy conversion and storage are believed to play important roles in future clean energy systems.[1] Hydrogen is an ideal clean energy material, and inexhaustible solar energy is highly attractive as a renewable energy resource. Thus, hydrogen production via photocatalytic water splitting is a highly desirable process and has received considerable attention during the past several years.[2−4] The oxygen evolution reaction (OER) largely determines the efficiency and practicability of those electrochemical processes due to the sluggish kinetics associated with the breaking of O−H bonds and the formation of O═O bonds.[5,6] Therefore, noble metal oxide catalysts (e.g., IrO_2 and RuO_2) are usually required to achieve acceptable performance,[7,8] but the rarity and high price of noble metals significantly limits their practical use in real devices. Therefore, the development of noble metal-free catalysts with low prices but high activities is heavily pursued.

The OER is a complicated process that involves multiple steps, and each step could be significantly rate limiting. In addition, the reaction mechanism may change significantly with a change in the material composition and particulate morphology. In an alkaline electrolyte, the reaction pathways of the OER over a catalyst include the adsorption of OH^- onto the catalyst surface, the oxidation of OH^- at the active sites, and the evolution of O_2 from the catalyst surface.[9] Although the exact adsorption sites are still not clear, it is undisputed that the catalyst should possess abundant redox active sites. Currently, two types of noble metal-free OER electrocatalysts have been exploited, i.e., carbon-based materials and transition metal oxides.[10−14] The catalytic activities of pristine carbon materials for the OER are low; they can be improved by doping the carbon materials with other elements. The enhanced activities of the doped-carbon materials for the OER originate from their dopant-related active sites.[10−12] One significant advantage of carbon-based electrocatalysts is the high electrical conductivity. However, precise tailoring of the surface properties of carbon materials is fairly difficult and may introduce significant challenges for the realization of reproducible catalytic activity. Furthermore, most carbon-based catalysts still have insufficient activity. Thus, composites with transition metal oxides that show high activities in the OER have also been extensively

Received: March 31, 2015
Accepted: July 29, 2015
Published: July 29, 2015

DOI: 10.1021/acsami.5b02810
ACS Appl. Mater. Interfaces 2015, 7, 17663−17670

studied.[15−17] The origin of the electrochemical activities of transition metal oxides is mainly related to the redox capabilities of the surface transition metal atoms.[10] Cobalt-based oxides are good candidates that have been extensively investigated for use as OER electrocatalysts in the literature.[18−22] In comparison with carbon materials, the surface properties of transition metal oxides can be much easier to tailor.

Recently, perovskite oxides have received considerable attention for application in many fields, including solid oxide fuel cells, ceramic oxygen separation membranes, solar cells, and metal−air batteries.[23−26] Such a wide application potential is mainly because perovskite is very versatile in elemental composition; more than 90% metallic elements in the periodic table can enter the perovskite lattice structure to alter its properties.[27] Different materials with a very large diversification of properties could be easily developed by carefully tailoring the elemental composition. Compared to conventional single oxides, perovskite oxides possess several advantages, such as high electrical conductivities, superior ion mobility, and redox properties.[27] All of these properties benefit the OER. Some perovskite oxides show high conductivities at room temperature that may reach several tens and even greater than 1000 S cm^{-1},[28] whereas single oxides usually have low conductivities of less than 1 S cm^{-1}.[29] A high conductivity is essential to minimizing the contact resistance. More recently, Suntivich et al. developed a descriptor for correlating the activity of perovskite catalysts for OER to its composition.[30] On the basis of the descriptor, $Ba_{0.5}Sr_{0.5}Co_{0.8}Fe_{0.2}O_{3-\delta}$ (BSCF), a material that showed very high activity for the oxygen reduction reaction at elevated temperature,[31] was proposed. It was a highly active electrocatalyst for the OER in alkaline electrolyte and delivered much higher intrinsic activity than the benchmark IrO_2.[30,32] However, BSCF was found to have an unstable surface morphology,[33,34] which introduces concerns about long-term operational stability. It suggests that new materials with high and stable performance are urgently needed.

In the present study, perovskite oxides with the specific composition of $SrM_{0.9}Ti_{0.1}O_{3-\delta}$ (M = Co, Fe) were synthesized, and their OER performances in alkaline electrolyte were comparatively investigated. Further comparisons with the state-of-the-art IrO_2 and BSCF catalysts were also conducted. $SrCo_{0.9}Ti_{0.1}O_{3-\delta}$ (SCT) delivered a comparable intrinsic activity as BSCF and a higher operational stability than BSCF and IrO_2, suggesting that SCT is a promising candidate as an electrocatalyst for the OER. Interestingly, although SFT also has good initial electrocatalytic activity for the OER, its performance deteriorated with time. An explanation for this difference was suggested. This study provides a strategy to choose appropriate B-site transition metal elements in perovskite catalysts for OER with stable activities.

2. EXPERIMENTAL SECTION

2.1. Catalysts Synthesis. Perovskite oxides were synthesized by a combined ethylenediaminetetraacetic acid-citric acid (EDTA-CA) complexing sol−gel method.[35] Taking the synthesis of $SrCo_{0.9}Ti_{0.1}O_{3-\delta}$ (SCT) as an example, tetrabutyl titanate ($C_{16}H_{36}O_4Ti$) and CA at a molar ratio of 1:5 were mixed in deionized water at 80 °C under vigorous stirring until the solution was clear, and stoichiometric amounts of $Sr(NO_3)_2$ and $Co(NO_3)_2{\cdot}6H_2O$ were then added to the above solution. EDTA and CA were added sequentially as complexing agents at a molar ratio of 1:1:2 for total metal ions to EDTA to CA, followed by $NH_3{\cdot}H_2O$, which was poured into the resulting solution to adjust the pH to 6−7. Then, the solution was heated at 100 °C with stirring until viscous. A black solid precursor was obtained by heating the viscous mixture at 250 °C for 5 h in an oven. Finally, the precursor was calcined at 1000 °C for 5 h in air to form SCT powder. The same calcination temperature and time was applied for $SrFe_{0.9}Ti_{0.1}O_{3-\delta}$ (SFT) and $Ba_{0.5}Sr_{0.5}Co_{0.8}Fe_{0.2}O_{3-\delta}$ (BSCF) powders. After cooling to room temperature, the powder was ground using an agate mortar and pestle by hand for subsequent characterizations and electrochemical measurements. Commercial IrO_2 was purchased from Aladdin Industrial Corporation, Shanghai, China.

2.2. Catalysts Characterization. Powder X-ray diffraction (XRD) patterns were collected on a Bruker D8 Advance X-ray diffractometer using Cu Kα radiation in a step-scan mode within the range of 10−90° (2θ) with intervals of 0.02°. Rietveld refinement of the XRD patterns was performed using the GSAS-EXPGUI software. The scanning electron microscopy (SEM) images were obtained on JEOL S4800 and Zeiss Neon 40EsB instruments. The high-resolution transmission electron microscopy (HRTEM) images were obtained on JEOL JEM-2100 instrument. N_2 adsorption/desorption isotherms were monitored at the temperature of liquid nitrogen on a Micromeritics TriStar II instrument. Brunauer−Emmett−Teller (BET) specific surface areas were acquired using adsorption data at a relative pressure range of P/P_0 = 0.05−0.35. The pore size distribution was determined using the Barrett−Joyner−Halenda (BJH) model based on the desorption data. The concentrations of metal ions in SCT, SFT, and BSCF samples were analyzed by inductively coupled plasma-optical emission spectrometer (ICP-OES) on an Optima 8300 instrument (PerkinElmer). Before the ICP measurement, 0.05 g of powder was completely dissolved in 10 mL of dilute hydrochloric acid, and then the solution was diluted using ultrapure water to 250 mL, leading to the resulting sample concentration of 200 mg L^{-1} for ICP test. X-ray photoelectron spectra (XPS) were recorded using a Kratos AXIS Ultra DLD system under UHV conditions with Al Kα X-ray, and the data were analyzed using the Kratos Vision and CasaXPS software.

2.3. Electrode Preparation and Electrochemical Measurements. The activity evaluation of the OER on various catalysts was performed under identical conditions with the same amount of catalyst loading. First, 10 mg of catalyst and 10 mg of carbon black (Super P, Alfa Aesar) were dispersed in a solution containing 1000 μL of absolute ethanol and 100 μL of Nafion solution (5.0 wt % in isopropanol and water solution) under sonication for 2 h. Then, 7 μL of the resulting suspension was pipetted onto a glassy carbon rotating disk electrode (GC-RDE, 0.196 cm^2, Pine Research Instrumentation, USA), leading to a catalyst loading of 0.32 mg cm^{-2}_{disk}, and it was then dried overnight in air to serve as the working electrode.

All of the electrochemical measurements were performed at room temperature in a three-electrode glass cell using Ag/AgCl in 4 M KCl solution and a platinum wire as the reference electrode and counter electrode, respectively. A 0.1 M KOH aqueous solution (pH ∼12.7) was used as the electrolyte, which was saturated with O_2 during the entire test to ensure the O_2/H_2O equilibrium. The working electrode was activated by potential cycling at least 25 times in the range of 0.2−1.0 V vs Ag/AgCl at a scan rate of 100 mV s^{-1} before collecting electrochemical data. Linear sweep voltammograms (LSVs) were obtained at a scan rate of 5 mV s^{-1} from 0.2 to 1.0 V vs Ag/AgCl using the RDE at 1600 rpm. For the catalyst stability test, the cyclic voltammograms (CVs) were recorded at a scan rate of 10 mV s^{-1} using the RDE at 1600 rpm for 100 cycles. Electrochemical impedance spectroscopy (EIS) was performed using an AC voltage with 5 mV amplitude within the frequency range from 1×10^4 to 1×10^{-1} Hz and recorded at 1.69, 1.71, 1.73, 1.75, and 1.77 V vs the reversible hydrogen electrode (RHE), respectively. All of the electrochemical data were recorded using a CHI 760E bipotentiostat (CH Instruments, Inc., USA). The measured potential values vs Ag/AgCl were converted to the RHE scale based on the Nernst eq 1 and corrected by *iR*-compensation according to eq 2.

$$E_{\mathrm{RHE}} = 0.205 + E_{\mathrm{Ag/AgCL(4MKCl)}} + 0.059 \times \mathrm{pH}_{\mathrm{electrolyte}} \quad (1)$$

$$E_{iR\,\mathrm{corrected}} = E - iR \quad (2)$$

DOI: 10.1021/acsami.5b02810
ACS Appl. Mater. Interfaces 2015, 7, 17663−17670

where i is the current and R is electrolyte ohmic resistance ($\approx$ 45 Ω) measured in the O_2-saturated 0.1 M KOH electrolyte. All potentials reported in this paper were referenced to the RHE.

3. RESULTS AND DISCUSSION

3.1. Characterization of the Catalysts. Figure 1 shows the room-temperature XRD patterns of the as-prepared SCT, SFT, and BSCF powders, calcined at high temperature and cooled to room temperature naturally in an ambient air atmosphere. For all three samples, the diffraction patterns can be well-indexed based on a cubic perovskite structure with space group $Pm\bar{3}m$. The corresponding SCT and SFT diffraction peaks were almost fully overlapped, suggesting very similar lattice parameters for both oxides. The diffraction peaks of BSCF shifted slightly to lower angles compared to those of SCT and SFT, indicating the larger lattice parameter. It coincides with the larger size of Ba^{2+} (1.61 Å) than Sr^{2+} (1.44 Å) in the A-site of perovskite. The lattice parameters, obtained from Rietveld refinement of the XRD patterns, were found to be $a = b = c$ = 3.865(4), 3.872(7) and 3.984(4) Å for SCT, SFT, and BSCF, respectively.

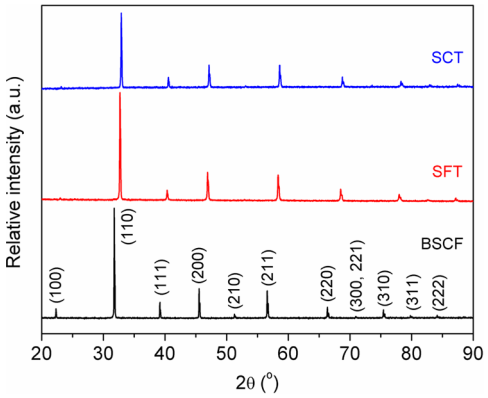

Figure 1. XRD patterns of the as-prepared SCT, SFT, and BSCF powders.

The particulate morphologies of the three samples were examined using SEM. Typical images are shown in Figure S1. All of them showed coarse particles with large grain sizes of several micrometers. The dense surface of the oxides implies that the materials are likely free from pores. To provide more information about the microstructure, we conducted N_2 adsorption/desorption isotherms at liquid nitrogen temperature. The specific surface areas calculated based on the BET method were 0.91, 0.86, and 0.43 $m^2\ g^{-1}$ for SCT, SFT, and BSCF, respectively. The pore size distribution profile clearly showed a lack of pores (Figure S2). A specific surface area of 139.84 $m^2\ g^{-1}$ was reached for the commercial IrO_2, and the corresponding BJH pore size distribution curve demonstrated the presence of 3.7 nm mesopores in the IrO_2 sample (Figure S3). The TEM images further confirmed the dense surface of three perovskite particles (insets in the Figure S4). As shown in Figure S4, HRTEM images revealed the lattice fringe spacing of d = 0.278, 0.281, and 0.289 nm for SCT, SFT, and BSCF, respectively, corresponding to the [110] crystal plane of the perovskite structure. The concentrations of metal ions in the prepared samples were identified by the ICP analysis with the data listed in Table S1. The mole ratios of elements in SCT, SFT, and BSCF samples were 10:9:1 (Sr: Co: Ti), 10:9:1 (Sr: Fe: Ti) and 5:5:8:2 (Ba: Sr: Co: Fe), respectively, which is in good agreement with the desired ratios.

3.2. Electrocatalytic Activities of the Catalysts for the OER. The OER activities of all of the catalysts were evaluated in a standard three-electrode cell containing O_2-saturated KOH aqueous solution (0.1 M) as the electrolyte using an RDE coated with a mixture of active material and carbon black (Super P). As mentioned previously, the perovskite catalysts show low specific surface areas, thus the addition of carbon could improve the contact between perovskite particles and current collector, and guarantee the full utilization of the efficient surface of perovskite particles.[36] The electrocatalytic activities of the electrodes for the OER were investigated using LSVs. Before collecting data, the working electrode was activated by potential cycling at least 25 times at a scan rate of 100 mV s^{-1}. To eliminate the effect of the potential cycling on the microstructure of the electrocatalyst, the basic characterizations of SCT (as an example) after the cycling of 25 times were studied by SEM, N_2 adsorption/desorption isotherms and XRD (Figure S5). Almost identical particle sizes, specific surface areas and crystallite sizes were obtained for SCT powder before and after the cycling of 25 times, suggesting no obvious effect occurred on the perovskite catalyst during the activation procedure. Typical LSV plots are shown in Figure 2a for the different catalysts on the RDEs at rotation speeds of 1600 rpm. Super P alone was also measured to rule out its possible contribution to the electrocatalytic activity of the

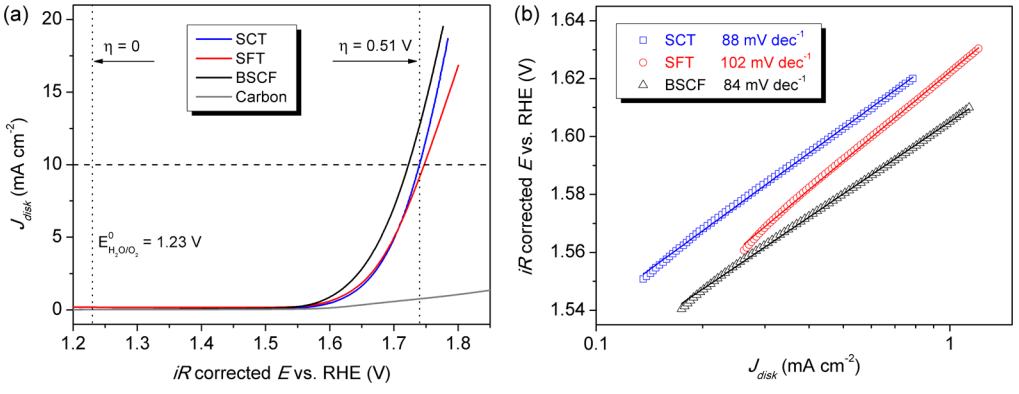

Figure 2. (a) LSV and (b) Tafel plots of the SCT, SFT, and BSCF electrocatalysts with an oxide catalyst loading of 0.32 mg cm^{-2}_{disk} supported on an RDE (1600 rpm) in O_2-saturated 0.1 M KOH electrolyte (scan rate: 5 mV s^{-1}). Background OER activity of carbon black (Super P) is shown for reference.

DOI: 10.1021/acsami.5b02810
ACS Appl. Mater. Interfaces 2015, 7, 17663−17670

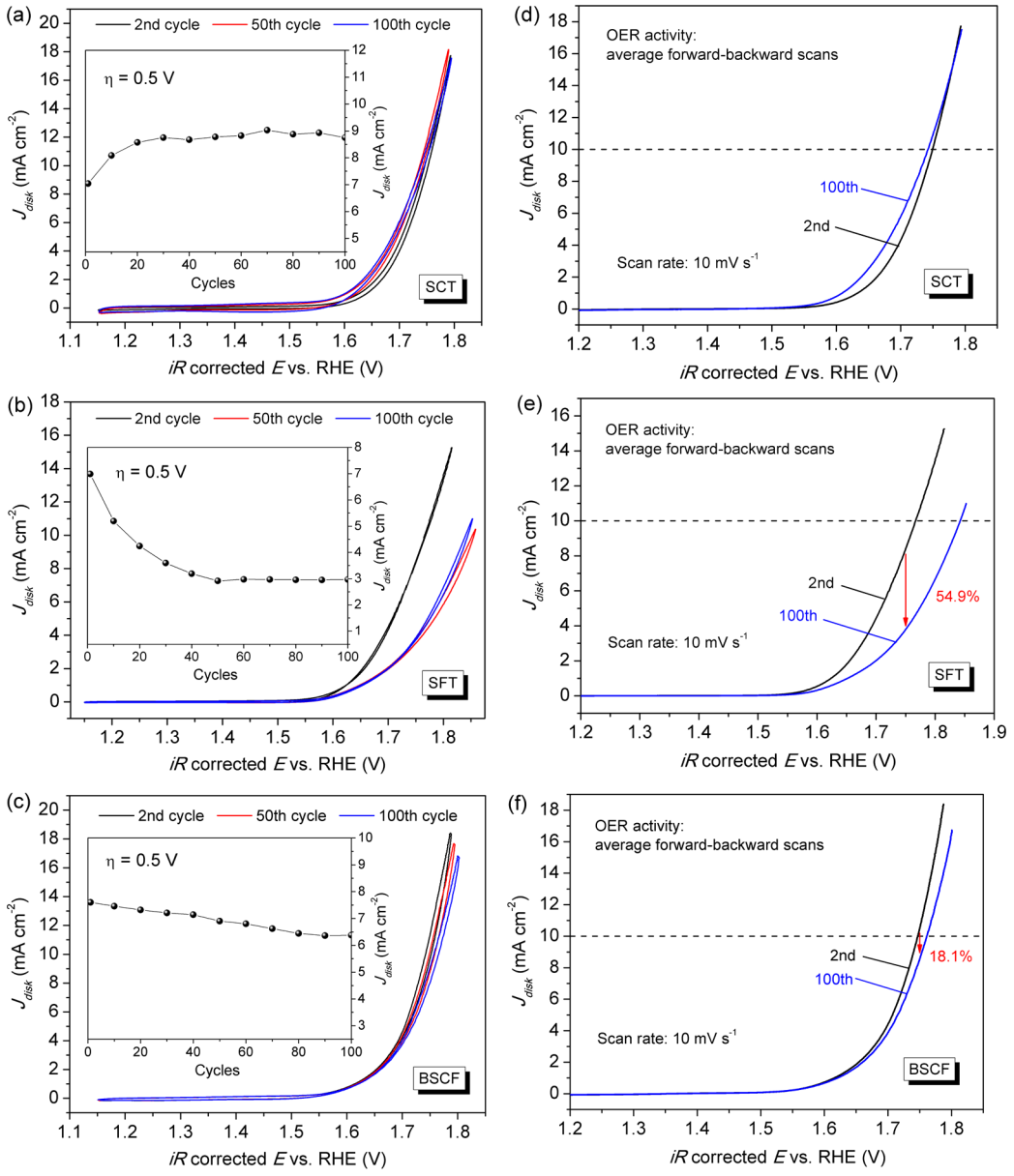

Figure 3. 2nd, 50th, and 100th CV scans of (a) SCT, (b) SFT, and (c) BSCF electrocatalysts with an oxide catalyst loading of 0.32 mg cm^{-2}_{disk} supported on an RDE (1600 rpm) in O_2-saturated 0.1 M KOH electrolyte under continuous potential sweeps (scan rate: 10 mV s^{-1}), and (inset) the current densities at η = 0.5 V under different scan cycles obtained from averaging currents in the forward and backward scans. (b–f) Corresponding capacitance-corrected OER activities of these three electrocatalysts in the 2nd and 100th cycles, respectively.

electrodes for the OER, and a negligible activity was demonstrated, as expected. It suggests that the carbon black did not contribute to the catalytic activity of oxides, assuming no significant chemical interaction appeared between the carbon phase and the oxide. Typically, the overpotential (η) to deliver a current density of 10 mA cm^{-2} is an important parameter to evaluate the activity of an OER electrocatalyst, which is expected for a 10% efficiency of a typical solar water-splitting device.[37] As shown in Figure 2a, the values of η were 0.51, 0.52, and 0.49 V for the SCT, SFT and BSCF electrodes, respectively for achieving the current density of 10 mA cm^{-2}. The above results denote that SCT and SFT catalysts are catalytically active for the OER in alkaline electrolyte. For all three perovskite-type oxide electrodes, although relatively lower absolute activities were obtained compared with the state-of-the-art noble-metal IrO_2 catalyst (Figure S6), the favorable specific activity, which reflects the intrinsic activity of a catalyst for the OER,[30] was demonstrated by considering the low specific surface area of the oxide powders. For example, the specific activities at η = 0.5 V were calculated with the values of 2.92, 2.91, 8.07, and 0.047 mA cm^{-2}_{oxide} for SCT, SFT, BSCF and IrO_2, respectively. SCT showed a similar initial intrinsic activity to SFT but lower than that of the benchmark BSCF electrocatalyst. Nonetheless, it was still approximately 60 times higher than that of the state-of-the-art IrO_2 electrocatalyst, suggesting its better intrinsic activity than IrO_2. To evaluate the OER kinetics of electrocatalysts, Tafel slope values were calculated from the Tafel plots of the current density dependence of the *i*R-corrected potential for the various electrodes. As shown in Figure 2b, the BSCF showed the lowest slope of 84 mV dec^{-1}, which matched well with the literature results.[38] SFT rendered the largest slope of 102 mV dec^{-1}. For

DOI: 10.1021/acsami.5b02810
ACS Appl. Mater. Interfaces 2015, 7, 17663–17670

the SCT catalyst, a slope value of 88 mV dec^{-1} was calculated, which is only slightly larger than that of BSCF and similar to that of the benchmark IrO_2 (89 mV dec^{-1}, Figure S7). The above results demonstrate the superior OER kinetics of SCT.

The variable transition metal cations in the B-site of perovskite oxides are the active sites for the OER.[10,30] On the basis of above results, both cobalt and iron could contribute to the OER. The A-site cations (Ba^{2+}, Sr^{2+}) did not directly participate in the OER, and the Ti^{4+} in the B-site of SCT and SFT was also likely not active for the OER because the redox reaction of Ti^{4+}/Ti^{3+} is unfavorable under the operation condition of the current study. It was reported that the generation of oxygen via the OER was partially from the lattice oxygen in the catalyst,[39] and the lower the average B−O bond energy (⟨B−O⟩), the easier the release of the lattice oxygen. The ⟨B−O⟩ within the lattice of perovskites was calculated according to the equations in the literature,[40] and the thermodynamic data were obtained using HSC software ver. 5.0. The values of ⟨B−O⟩ in the SCT, SFT, and BSCF were estimated to be −191.3, −200.2, and −179.0 kJ mol^{-1}, respectively. Therefore, the higher activity of BSCF than SCT and SFT could result in part from the lower ⟨B−O⟩ in the former oxide. Additionally, the slightly higher catalytic performance of BSCF for the OER than SCT could also be related to the higher concentration of transition metal elements (Co and Fe) in the B-site of the perovskite in BSCF. Recently, Suntivich et al. demonstrated that the OER activity of many perovskite oxides are closely related to the e_g electron filling of surface transition metal cations in the oxides, which hinges on the oxidation state of the B-site cations and the spin state of the electrons. The correlation between the electrocatalytic activity of $SrM_{0.9}Ti_{0.1}O_{3-\delta}$ (M = Co, Fe) and this principle will be discussed later.

3.3. Durability of the Catalysts for the OER. In addition to the activity, the durability is also a large concern for the practical application of electrocatalysts for the OER. The electrodes usually operate in a highly corrosive environment of liquid alkaline electrolyte for the OER, while the dissolution of oxides into the liquid electrolyte or the phase transition could cause a degradation of the electrode performance. To obtain information about the operational stability of the various electrodes in alkaline electrolyte, we carried out 100 continuous potential cycles at a scan rate of 10 mV s^{-1}. Figure 3a−c shows the CV curves at different cycles for three perovskite oxide catalysts, and the capacitance-corrected OER activities of these three electrocatalysts based on CVs at the second and 100th cycles was correspondingly shown in Figure 3d−f, respectively. The details about the capacitive correction could be found in Figure S8. The SCT electrocatalyst delivered the most stable performance among the three catalysts. The current at η = 0.5 V slowly increased during the first 20 scan cycles, and then remained very stable until the 100th cycle. To compare the OER activity in the second and 100th cycles, we obtained almost identical current at high potentials, while a smaller potential of 1.74 V was demonstrated for the 100th cycle compared with 1.75 V for the second cycle at 10 mA cm^{-2} (Figure 3d), implying an improved activity was likely acquired after the continuous CVs sweeps. To obtain further kinetic information, the Tafel plots of SCT were also drawn according to the second and 100th cycles (Figure S9), a slightly smaller Tafel slope of 85 mV dec^{-1} for the 100th cycle compared to that of the second cycle (87 mV dec^{-1}) was observed, indicating that the activity of the SCT catalyst for the OER improved after100 CVs scans. For the SFT electrode, an obvious decay in performance with cycling was demonstrated, as shown in Figure 3b, and the total attenuation of the current density at 1.75 V after 100 cycles was 54.9% (Figure 3e), suggesting poor operational stability of SFT for the OER in alkaline electrolyte. Even the BSCF electrode, with its well-known high activity for the OER, showed a slight deterioration with the cycling, which could result from the partial change in its structure.[38] For example, after 100 continuous potential sweeps, the current density at 1.75 V showed a decrease from 10.5 to 8.6 mA cm^{-2} with a reduction of 18.1%. The stability of the commercial IrO_2 catalyst was also compared, as shown in Figures S10 and S11. A reduction of 39.6% in current at 1.65 V was detected, which is in good agreement with the literature.[11,19,22] The reason for such degradation is the formation of unstable Ir(VI) (e.g., water-soluble IrO_4^{2-}) due to the oxidation of surface Ir(IV).[41,42]

To gain insight into the different cyclic performances of the three perovskite catalysts during the oxygen evolution reaction, we conducted EIS analyses of the electrode materials before and after 100 cycles at η = 0.5 V (Figure 4 and Figure S12). As

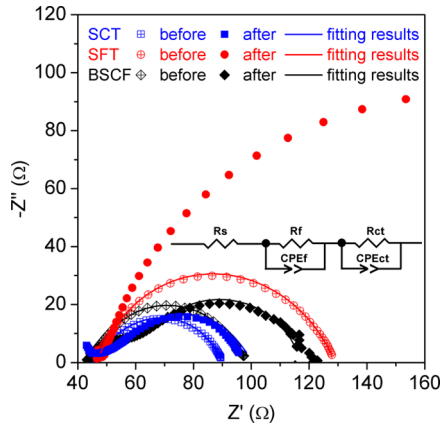

Figure 4. EIS Nyquist plots of SCT, SFT, and BSCF electrodes before and after 100 cycles recorded at 1.73 V under the influence of an AC voltage of 5 mV with an RDE rotating rate of 1600 rpm. Inset: the corresponding equivalent circuit diagram.

shown in Figure 4, compared to the SFT electrode before 100 cycles, an apparently different EIS plot was presented for the SFT after 100 cycles, suggesting a significant change in OER activity of SFT after the stability test. In contrast, minor change happened for EIS plots of SCT and BSCF electrodes after 100 cycles. To better analyze the process of electrode reactions, we carried out EIS on SCT electrode (as an example) at different potentials with the results shown in Figure S13. At high and medium frequencies, five curves almost overlaid, indicating the impedance was related to the dielectric properties and the resistivity of the oxide film.[21,43] The arcs at low frequency increased with the decrease in applied potential, which could be attributed to the impedance caused by the OER. To further comprehend the kinetic of three different perovskites for OER, we fitted the measured EIS data using an equivalent circuit diagram consisting of an electrolyte resistance (R_s), an oxide film resistance (R_f), a charge-transfer resistance (R_{ct}), and two constant-phase elements (CPE_f and CPE_{ct}).[43] EIS curves obtained from the experiment were fitted well with the applied equivalent circuit, and the corresponding fitting results of impedance are listed in Table S2. It is worth mentioning that

DOI: 10.1021/acsami.5b02810
ACS Appl. Mater. Interfaces 2015, 7, 17663−17670

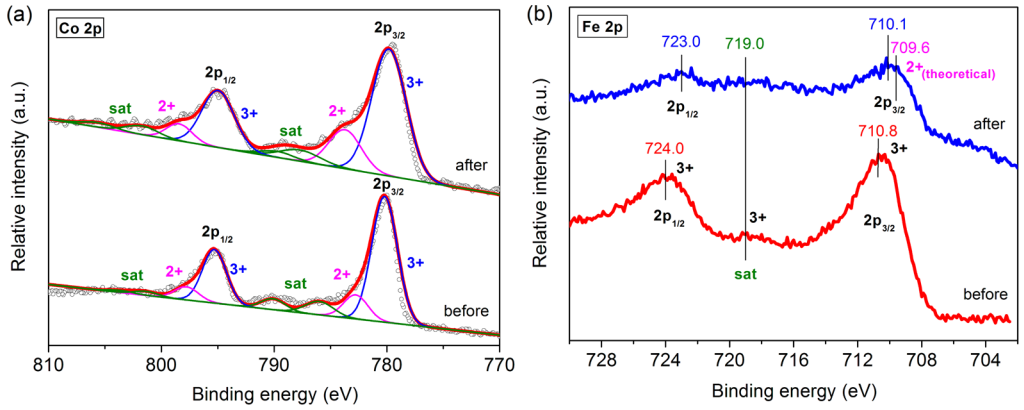

Figure 5. XPS spectra of (a) Co 2p on SCT and (b) Fe 2p on SFT before and after the 100 CV scans.

the EIS data of SFT electrode after 100 cycles could not be fitted because of the distinct increment in R_{ct}. Nevertheless, the arc at low frequency increased obviously after the cycling, which demonstrated the attenuation in OER activity of SFT. R_{ct} is a critical factor in the evaluation of the electrochemical performance of the catalysts. As shown in Figure 4 and Table S2, before 100 cycles, the R_{ct} of SCT (34.52 Ω) is comparable to that of BSCF (38.55 Ω), and SFT exhibited a relatively larger R_{ct} (60.11 Ω) than both SCT and BSCF. This result suggests that the SCT electrode possessed excellent charge transfer ability. After 100 cycles, a significant increase in the R_{ct} of SFT was found, indicating the charge transport efficiency dramatically decreased for SFT electrode. For the BSCF catalyst, there was an obvious increase of 32% in R_{ct} (50.96 Ω) after continuous potential sweeps. For the SCT electrode, an almost unchanged R_{ct} (33.13 Ω) was observed after 100 cycles. These findings agree well with the CV sweeping results, shown in Figure 3.

To obtain information to explain the different durability performances of the oxides, both SCT and SFT electrodes before and after the CVs scans were subjected to XPS characterization, and the results are shown in Figure 5. For a clear comparison of the samples after 100 cycles, the intensities of the fresh SCT and SFT spectra was scaled to 1/3 and 1/2 of the original data, respectively. Figure 5a shows the XPS spectra of the Co 2p on the SCT surface before and after the 100 CV scans and the corresponding deconvolutions for the $2p_{1/2}$ and $2p_{3/2}$. Both Co $2p_{1/2}$ and $2p_{3/2}$ can be deconvoluted to four peaks assigned to Co^{3+}, Co^{2+}, and Co satellite (sat, including the two peaks marked green in the figure). Compared with the fresh SCT, the ratio of Co^{3+} to Co^{2+} based on the peak area intensity decreased from 5.00 to 3.63 in the SCT after the CV tests. In other words, the average cobalt oxidation states were approximately 2.83 and 2.78 in fresh and used SCT, respectively. This result suggests that the Co ions were slightly reduced during the continuous CVs sweeps. Recently, Suntivich et al. reported that the catalytic activity of a perovskite oxide for the OER was highly dependent on the occupation of e_g orbital in the 3d electron of the B-site transition metal element, and then, a volcano-shape plot was proposed. It was believed that the best performance was achieved when the surface cation e_g occupancy of the transition metal elements was approximately 1.2.[30] Generally, it is accepted that the spin state of Co^{3+} is intermediate-spin (IS),[30,38] although it is still under debate. Thus, we assume Co^{3+} exists as IS ($e_g\uparrow 3t_{2g}\uparrow 2t_{2g}\downarrow$) in this study. The Co^{2+} spin state is high-spin (HS, $2e_g\uparrow 3t_{2g}\uparrow 2t_{2g}\downarrow$). On the basis of the ratio of Co^{3+} to Co^{2+} in the fresh SCT, the e_g electron filling of Co was calculated to be 1.16, which was slightly lower than the optimized value of 1.2 (BSCF).[30] This behavior may also contribute to the difference in the OER activity between SCT and BSCF (Figure 2). For the SCT after the 100 CVs, the e_g electron filling of Co was calculated to be 1.22, which was slightly larger than 1.2, but much closer to 1.2 than 1.16 (the cobalt ion in the fresh SCT). This result indicates that the e_g occupation of Co in SCT after 100 CV cycles was altered to a state that had better OER activity; thus, the slightly improved catalytic activity was expected. In the case of Fe 2p, the XPS spectra are always divided into two peaks because of the different spin−orbit coupling involving Fe $2p_{1/2}$ and Fe $2p_{3/2}$ (Figure 5b). Generally, the analysis of the Fe 2p peaks for various chemical states is very difficult because of the large background; however, the satellite peak at a binding energy (BE) of ∼719.0 eV are important to the identification of the valence state of Fe. As shown in Figure 5b, for the fresh SFT, this satellite peak and the typical Fe $2p_{3/2}$ peak at 710.8 eV and the Fe $2p_{1/2}$ peak at 724.0 eV were observed, indicating the presence of Fe^{3+} in the fresh SFT. For the SFT after the CV tests, the spectrum of Fe 2p was broader than that of the fresh one, and the peaks shifted to lower BEs. In addition, the satellite peak at ∼719.0 eV that is a major indicator of Fe^{3+} almost disappeared. Refer to the theoretical peak of Fe^{2+} and the analysis in the literatures, the above results indicated the existence of two iron oxidation states (Fe^{2+} and Fe^{3+}) in the used SFT that have different but unresolvable BEs.[44] The iron ion typically exists as HS (Fe^{2+}: $2e_g\uparrow e_g\downarrow 3t_{2g}\uparrow$, Fe^{3+}: $2e_g\uparrow 3t_{2g}\uparrow$) at ambient conditions.[45] The appearance of Fe^{2+} in the used SFT catalyst is a negative factor for OER activity due to the larger value of e_g electron filling for Fe^{2+} than Fe^{3+}. Consequently, the reduced activity for SFT with cycling was expected. For BSCF, assuming the same trend for cobalt and iron ions in BSCF, the overall performance is an average of the two opposite effects. It seems that the reduced activity for the iron played a slightly more significant role than the increased activity from the cobalt. As a result, a slight decrease in activity for the OER was observed for BSCF after 100 cycles.

To further support the superior durability behavior of the SCT catalyst, the chronoamperometric response was conducted at a constant potential of 1.83 V to ensure an initial current of 10 mA cm^{-2}. For comparison, the benchmark IrO_2 was also tested. As shown in Figure 6, the IrO_2 catalyst exhibited an anode current loss of 16.1% after continuous operation for 10 h. However, SCT offered a stable current over the same

DOI: 10.1021/acsami.5b02810
ACS Appl. Mater. Interfaces 2015, 7, 17663−17670

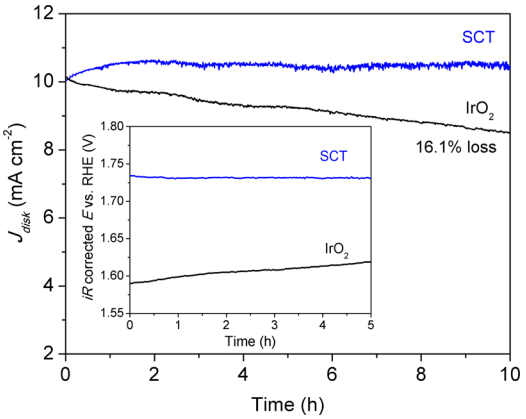

Figure 6. Chronoamperometric responses of SCT and IrO_2 electrodes at constant potentials of 1.83 V (for SCT) and 1.74 V (for IrO_2) to ensure an initial current density of 10 mA cm^{-2}. Inset: chronopotentiometric responses of SCT and IrO_2 electrodes at a constant current density of 10 mA cm^{-2}.

operational period (10 h). The inset in the Figure 6 shows the chronopotentiometric responses of SCT and IrO_2 catalysts at a constant current of 10 mA cm^{-2}. SCT affords an almost unchanged operating potential of 1.73 V within 5 h, whereas the potential increased obviously with time for IrO_2 catalyst under the exact same condition, suggesting the deactivation of IrO_2. The above results agreed well with the conclusion from the continuous potential CVs sweeps. However, the carbon was probably particularly damageable during the stability test, which may have a potential influence on the produced oxidation current. Therefore, the chronoamperometric response of SCT alone without the addition of carbon black was conducted. In addition, 100 continuous potential cycles on SCT alone were also carried out. As shown in Figure S14, both electrochemical tests demonstrate the superb stability of SCT alone. These results further confirm the inherently stable operation of SCT in alkaline medium, indicating the potential for application and providing a new avenue for the development of OER catalysts in the future.

4. CONCLUSIONS

In summary, we have synthesized $SrM_{0.9}Ti_{0.1}O_3$ (M = Co, Fe) catalysts through a traditional sol–gel method and investigated them as potential electrocatalysts for the oxygen evolution reaction in alkaline media at room temperature. The SCT catalyst exhibited a favorable OER intrinsic activity, which was even comparable to the benchmark BSCF perovskite oxide, but showed better durability than BSCF and commercial IrO_2 catalysts. Such favorable electrochemical activity is attributed to the low average B–O bond energy, good charge transfer ability, and optimal e_g electron filling (1.16 and 1.22 for the SCT catalyst before and after the continuous potential CV sweeps, respectively). For the SFT catalyst, although a favorable catalytic activity was obtained, much worse stability was demonstrated. The increase in the Fe^{2+} content in the surface layer of the SFT oxide during operation resulted in a larger value of e_g electron filling, which may have led to the reduced activity for the OER. This study emphasized the significance of the B-site transition metal elements in perovskite to achieve both high catalytic activity and stable performance for the OER. More specifically, cobalt-based perovskites are promising catalysts for the OER. Considering the more abundant resources, cheaper price and better environmentally friendliness of iron than cobalt, the development of iron-based perovskites with stable and favorable performance for OER is highly desired. Stabilizing the valence state of iron in the perovskite oxide is the key to achieving stable performance. The modification of iron-based perovskite with a foreign B-site element to alter the electron environment of iron in the perovskite lattice may be a useful strategy to stabilize Fe^{3+}, and related works will be conducted in the near future.

■ ASSOCIATED CONTENT

Supporting Information

The Supporting Information is available free of charge on the ACS Publications website at DOI: 10.1021/acsami.5b02810.

SEM and HRTEM images of SCT, SFT, and BSCF catalysts; concentrations of the metal ions in prepared SCT, SFT, and BSCF powders; nitrogen adsorption/desorption isotherm patterns and corresponding BJH pore size distribution curves of SCT, SFT, BSCF, and IrO_2 catalysts; XRD patterns of SCT; OER activity and stability of IrO_2 catalyst; additional OER performance and stability data of SCT; additional EIS plots of SCT, SFT and BSCF; capacitive correction of the OER activity based on the CV tests (PDF)

■ AUTHOR INFORMATION

Corresponding Author

*E-mail: zongping.shao@curtin.edu.au. Tel.: +61 8 92664702. Fax: +61 8 92662681.

Notes

The authors declare no competing financial interest.

■ ACKNOWLEDGMENTS

The work was supported by the Australia Research Council (ARC) Future Fellowship under the contract FT100100134, and the ARC Discovery Project under the contract DP150104365. C.S. acknowledges Curtin University for a postdoctoral fellowship. The authors acknowledge the use of Curtin University's Microscopy & Microanalysis Facility, whose instrumentation has been partially funded by the University, State and Commonwealth Governments. The authors also acknowledge the WA X-ray Surface Analysis Facility, which has funded by the ARC LIEF grant LE120100026.

■ REFERENCES

(1) Li, L.; Wu, Z.; Yuan, S.; Zhang, X. B. Advances and Challenges for Flexible Energy Storage and Conversion Devices and Systems. *Energy Environ. Sci.* **2014**, *7*, 2101–2122.

(2) Walter, M. G.; Warren, E. L.; McKone, J. R.; Boettcher, S. W.; Mi, Q.; Santori, E. A.; Lewis, N. S. Solar Water Splitting Cells. *Chem. Rev.* **2010**, *110*, 6446–6473.

(3) Lu, D.; Takata, T.; Saito, N.; Inoue, Y.; Domen, K. Photocatalyst Releasing Hydrogen from Water. *Nature* **2006**, *440*, 295.

(4) Wang, P.; Wang, D.; Lin, J.; Li, X.; Peng, C.; Gao, X.; Huang, Q.; Wang, J.; Xu, H.; Fan, C. Lattice Defect-Enhanced Hydrogen Production in Nanostructured Hematite-Based Photoelectrochemical Device. *ACS Appl. Mater. Interfaces* **2012**, *4*, 2295–2302.

(5) Mirzakulova, E.; Khatmullin, R.; Walpita, J.; Corrigan, T.; Vargas-Barbosa, N. M.; Vyas, S.; Oottikkal, S.; Manzer, S. F.; Hadad, C. M.; Glusac, K. D. Electrode-Assisted Catalytic Water Oxidation by a Flavin Derivative. *Nat. Chem.* **2012**, *4*, 794–801.

(6) Lee, S. W.; Carlton, C.; Risch, M.; Surendranath, Y.; Chen, S.; Furutsuki, S.; Yamada, A.; Nocera, D. G.; Shao-Horn, Y. The Nature of

DOI: 10.1021/acsami.5b02810
ACS Appl. Mater. Interfaces 2015, 7, 17663–17670

Lithium Battery Materials under Oxygen Evolution Reaction Conditions. *J. Am. Chem. Soc.* **2012**, *134*, 16959−16962.
(7) Siracusano, S.; Van Dijk, N.; Payne-Johnson, E.; Baglio, V.; Aricò, A. S. Nanosized IrO_x and $IrRuO_x$ Electrocatalysts for the O_2 Evolution Reaction in PEM Water Electrolysers. *Appl. Catal., B* **2015**, *164*, 488−495.
(8) Cao, R.; Lai, W.; Du, P. Catalytic Water Oxidation at Single Metal Sites. *Energy Environ. Sci.* **2012**, *5*, 8134−8157.
(9) Bockrls, J.; Otagawa, T. Mechanism of Oxygen Evolution on Perovskites. *J. Phys. Chem.* **1983**, *87*, 2960−2971.
(10) Wang, Z. L.; Xu, D.; Xu, J. J.; Zhang, X. B. Oxygen Electrocatalysts in Metal−Air Batteries: from Aqueous to Nonaqueous Electrolytes. *Chem. Soc. Rev.* **2014**, *43*, 7746−7786.
(11) Ma, T. Y.; Dai, S.; Jaroniec, M.; Qiao, S. Z. Graphitic Carbon Nitride Nanosheet−Carbon Nanotube Three-Dimensional Porous Composites as High-Performance Oxygen Evolution Electrocatalysts. *Angew. Chem., Int. Ed.* **2014**, *53*, 7281−7285.
(12) Zhao, Y.; Nakamura, R.; Kamiya, K.; Nakanishi, S.; Hashimoto, K. Nitrogen−Doped Carbon Nanomaterials as Non-Metal Electrocatalysts for Water Oxidation. *Nat. Commun.* **2013**, *4* (2390), 1−7.
(13) Cheng, F.; Shen, J.; Peng, B.; Pan, Y.; Tao, Z.; Chen, J. Rapid Room−Temperature Synthesis of Nanocrystalline Spinels as Oxygen Reduction and Evolution Electrocatalysts. *Nat. Chem.* **2011**, *3*, 79−84.
(14) Ge, X.; Liu, Y.; Goh, F. W. T.; Hor, T. S. A.; Zong, Y.; Xiao, P.; Zhang, Z.; Lim, S. H.; Li, B.; Wang, X.; Liu, Z. Dual-Phase Spinel $MnCo_2O_4$ and Spinel $MnCo_2O_4$/Nanocarbon Hybrids for Electrocatalytic Oxygen Reduction and Evolution. *ACS Appl. Mater. Interfaces* **2014**, *6*, 12684−12691.
(15) Chen, S.; Duan, J.; Han, W.; Qiao, S. Z. A Graphene−MnO_2 Framework as a New Generation of Three-Dimensional Oxygen Evolution Promoter. *Chem. Commun.* **2014**, *50*, 207−209.
(16) Yu, X.; Hua, T.; Liu, X.; Yan, Z.; Xu, P.; Du, P. Nickel-Based Thin Film on Multiwalled Carbon Nanotubes as an Efficient Bifunctional Electrocatalyst for Water Splitting. *ACS Appl. Mater. Interfaces* **2014**, *6*, 15395−15402.
(17) Mao, S.; Wen, Z.; Huang, T.; Hou, Y.; Chen, J. High-Performance Bi-Functional Electrocatalysts of 3D Crumpled Graphene−Cobalt Oxide Nanohybrids for Oxygen Reduction and Evolution Reactions. *Energy Environ. Sci.* **2014**, *7*, 609−616.
(18) Liang, Y.; Li, Y.; Wang, H.; Zhou, J.; Wang, J.; Regier, T.; Dai, H. Co_3O_4 Nanocrystals on Graphene as a Synergistic Catalyst for Oxygen Reduction Reaction. *Nat. Mater.* **2011**, *10*, 780−786.
(19) Liu, X.; Chang, Z.; Luo, L.; Xu, T.; Lei, X.; Liu, J.; Sun, X. Hierarchical $Zn_xCo_{3-x}O_4$ Nanoarrays with High Activity for Electrocatalytic Oxygen Evolution. *Chem. Mater.* **2014**, *26*, 1889−1895.
(20) Grimaud, A.; May, K. J.; Carlton, C. E.; Lee, Y. L.; Risch, M.; Hong, W. T.; Zhou, J.; Shao-Horn, Y. Double Perovskites as a Family of Highly Active Catalysts for Oxygen Evolution in Alkaline Solution. *Nat. Commun.* **2013**, *4* (2439), 1−7.
(21) Jin, C.; Lu, F.; Cao, X.; Yang, Z.; Yang, R. Facile Synthesis and Excellent Electrochemical Properties of $NiCo_2O_4$ Spinel Nanowire Arrays as a Bifunctional Catalyst for the Oxygen Reduction and Evolution Reaction. *J. Mater. Chem. A* **2013**, *1*, 12170−12177.
(22) Ma, T. Y.; Dai, S.; Jaroniec, M.; Qiao, S. Z. Synthesis of Highly Active and Stable Spinel-Type Oxygen Evolution Electrocatalysts by a Rapid Inorganic Self-Templating Method. *Chem. - Eur. J.* **2014**, *20*, 12669−12676.
(23) Yang, C.; Li, J.; Lin, Y.; Liu, J.; Chen, F.; Liu, M. In Situ Fabrication of CoFe Alloy Nanoparticles Structured $(Pr_{0.4}Sr_{0.6})_3(Fe_{0.85}Nb_{0.15})_2O_7$ Ceramic Anode for Direct Hydrocarbon Solid Oxide Fuel Cells. *Nano Energy* **2015**, *11*, 704−710.
(24) Zhang, Z.; Chen, Y.; Tadé, M. O.; Hao, Y.; Liu, S.; Shao, Z. Tin-Doped Perovskite Mixed Conducting Membrane for Efficient Air Separation. *J. Mater. Chem. A* **2014**, *2*, 9666−9674.
(25) Grinberg, I.; West, D. V.; Torres, M.; Gou, G.; Stein, D. M.; Wu, L.; Chen, G.; Gallo, E. M.; Akbashev, A. R.; Davies, P. K.; Spanier, J. E.; Rappe, A. M. Perovskite Oxides for Visible-Light-Absorbing Ferroelectric and Photovoltaic Materials. *Nature* **2013**, *503*, 509−512.
(26) Jung, K.-N.; Jung, J.-H.; Im, W. B.; Yoon, S.; Shin, K.-H.; Lee, J.-W. Doped Lanthanum Nickelates with a Layered Perovskite Structure as Bifunctional Cathode Catalysts for Rechargeable Metal−Air Batteries. *ACS Appl. Mater. Interfaces* **2013**, *5*, 9902−9907.
(27) Peña, M. A.; Fierro, J. L. G. Chemical Structures and Performance of Perovskite Oxides. *Chem. Rev.* **2001**, *101*, 1981−2017.
(28) Kozuka, H.; Yamada, H.; Hishida, T.; Yamagiwa, K.; Ohbayashia, K.; Koumoto, K. Electronic Transport Properties of the Perovskite-Type Oxides $La_{1-x}Sr_xCoO_{3\pm\delta}$. *J. Mater. Chem.* **2012**, *22*, 20217−20222.
(29) Sakamoto, S.; Yoshinaka, M.; Hirota, K.; Yamaguchi, O. Fabrication, Mechanical Properties, and Electrical Conductivity of Co_3O_4 Ceramics. *J. Am. Ceram. Soc.* **1997**, *80*, 267−268.
(30) Suntivich, J.; May, K. J.; Gasteiger, H. A.; Goodenough, J. B.; Shao-Horn, Y. Perovskite Oxide Optimized for Oxygen Evolution Catalysis from Molecular Orbital Principles. *Science* **2011**, *334*, 1383−1385.
(31) Shao, Z.; Haile, S. M. A High-Performance Cathode for the Next Generation of Solid-Oxide Fuel Cells. *Nature* **2004**, *431*, 170−173.
(32) Jung, J.; Jeong, H. Y.; Kim, M. G.; Nam, G.; Park, J.; Cho, J. Fabrication of $Ba_{0.5}Sr_{0.5}Co_{0.8}Fe_{0.2}O_{3-\delta}$ Catalysts with Enhanced Electrochemical Performance by Removing an Inherent Heterogeneous Surface Film Layer. *Adv. Mater.* **2015**, *27*, 266−271.
(33) May, K. J.; Carlton, C. E.; Stoerzinger, K. A.; Risch, M.; Suntivich, J.; Lee, Y. L.; Grimaud, A.; Shao-Horn, Y. Influence of Oxygen Evolution during Water Oxidation on the Surface of Perovskite Oxide Catalysts. *J. Phys. Chem. Lett.* **2012**, *3*, 3264−3270.
(34) Risch, M.; Grimaud, A.; May, K. J.; Stoerzinger, K. A.; Chen, T. J.; Mansour, A. N.; Shao-Horn, Y. Structural Changes of Cobalt-Based Perovskites upon Water Oxidation Investigated by EXAFS. *J. Phys. Chem. C* **2013**, *117*, 8628−8635.
(35) Gu, H.; Ran, R.; Zhou, W.; Shao, Z. Anode-Supported ScSZ-Electrolyte SOFC with Whole Cell Materials from Combined EDTA−Citrate Complexing Synthesis Process. *J. Power Sources* **2007**, *172*, 704−712.
(36) Poux, T.; Napolskiy, F. S.; Dintzer, T.; Kéranguéven, G.; Istomin, S. Y.; Tsirlina, G. A.; Antipov, E. V.; Savinova, E. R. Dual Role of Carbon in the Catalytic Layers of Perovskite/Carbon Composites for the Electrocatalytic Oxygen Reduction Reaction. *Catal. Today* **2012**, *189*, 83−92.
(37) McCrory, C. C. L.; Jung, S.; Peters, J. C.; Jaramillo, T. F. Benchmarking Heterogeneous Electrocatalysts for the Oxygen Evolution Reaction. *J. Am. Chem. Soc.* **2013**, *135*, 16977−16987.
(38) Zhu, Y.; Zhou, W.; Chen, Z. G.; Chen, Y.; Su, C.; Tadé, M. O.; Shao, Z. $SrNb_{0.1}Co_{0.7}Fe_{0.2}O_{3-\delta}$ Perovskite as a Next-Generation Electrocatalyst for Oxygen Evolution in Alkaline Solution. *Angew. Chem., Int. Ed.* **2015**, *54*, 3897−3901.
(39) Hardin, W. G.; Slanac, D. A.; Wang, X.; Dai, S.; Johnston, K. P.; Stevenson, K. J. Highly Active, Nonprecious Metal Perovskite Electrocatalysts for Bifunctional Metal−Air Battery Electrodes. *J. Phys. Chem. Lett.* **2013**, *4*, 1254−1259.
(40) Konysheva, E. Yu.; Xu, X.; Irvine, J. T. S. On the Existence of A-Site Deficiency in Perovskites and Its Relation to the Electrochemical Performance. *Adv. Mater.* **2012**, *24*, 528−532.
(41) Rasiyah, P.; Tseung, A. C. C. The Role of the Lower Metal Oxide/Higher Metal Oxide Couple in Oxygen Evolution Reactions. *J. Electrochem. Soc.* **1984**, *131*, 803−808.
(42) KStz, R.; Neff, H.; Stucki, S. Anodic Iridium Oxide Films. *J. Electrochem. Soc.* **1984**, *131*, 72−77.
(43) Singh, R. N.; Kumar, M.; Sinha, A. S. K. Novel $Fe_xCr_{2-x}(MoO_4)_3$ Electrocatalysts for Oxygen Evolution Reaction. *Int. J. Hydrogen Energy* **2012**, *37*, 15117−15124.
(44) Gao, Y.; Chambers, S. A. Heteroepitaxial Growth of α-Fe_2O_3, γ-Fe_2O_3 and Fe_3O_4 Thin Films by Oxygen-Plasma-Assisted Molecular Beam Epitaxy. *J. Cryst. Growth* **1997**, *174*, 446−454.
(45) Bengtson, A.; Li, J.; Morgan, D. Mössbauer Modeling to Interpret the Spin State of Iron in $(Mg,Fe)SiO_3$ Perovskite. *Geophys. Res. Lett.* **2009**, *36*, L15301.

DOI: 10.1021/acsami.5b02810
ACS Appl. Mater. Interfaces 2015, 7, 17663−17670